Toward the optimization of double-pulse LIBS underwater: effects of experimental parameters on the reproducibility and dynamics of laser-induced cavitation bubble

Gabriele Cristoforetti,[1,*] Marco Tiberi,[2] Andrea Simonelli,[2] Paolo Marsili,[2] and Francesco Giammanco[2]

[1]ILIL, National Institute of Optics, Research Area of National Research Council, Via G. Moruzzi 1, 56124 Pisa, Italy

[2]Department of Physics "E. Fermi," University of Pisa, Largo Bruno Pontecorvo 3, 56127 Pisa, Italy

*Corresponding author: gabriele.cristoforetti@cnr.it

Received 19 September 2011; revised 10 January 2012; accepted 17 January 2012; posted 17 January 2012 (Doc. ID 154898); published 7 February 2012

Double-pulse laser-induced breakdown spectroscopy (LIBS) was recently proposed for the analysis of underwater samples, since it overcomes the drawbacks of rapid plasma quenching and of large continuum emission, typical of single-pulse ablation. Despite the attractiveness of the method, this approach suffers nevertheless from a poor spectroscopic reproducibility, which is partially due to the scarce reproducibility of the cavitation bubble induced by the first laser pulse, since pressure and dimensions of the bubble strongly affect plasma emission. In this work, we investigated the reproducibility and the dynamics of the cavitation bubble induced on a solid target in water, and how they depend on pulse duration, energy, and wavelength, as well as on target composition. Results are discussed in terms of the effects on the laser ablation process produced by the crater formation and by the interaction of the laser pulse with floating particles and gas bubbles. This work, preliminary to the optimization of the spectroscopic signal, provides an insight of the phenomena occurring during laser ablation in water, together with useful information for the choice of the laser source to be used in the apparatus.

OCIS codes: 350.5400, 300.6365, 010.7340, 110.6915, 290.5850.

1. Introduction

In the last decade, the interest in laser-induced breakdown spectroscopy (LIBS) technique rapidly and impressively rose, leading to a deeper understanding of the physical processes involved, to the development of suitable apparatus, and to the suggestion of applications in a widespread range of fields. One of the perhaps more original applications proposed is the analysis of samples located underwater, which is particularly attractive for objects that can be difficultly removed from water, such as wrecks or large artworks, or for performing a rapid screening of large amounts of samples, such as for soils or sediments mapping. For this kind of application, the traditional single-pulse LIBS setup is not suitable, because the plasma induced in water is rapidly quenched in a few hundred nanoseconds, since a large part of its energy is dissipated via shock waves, heat conduction, or water molecule dissociation, and because the spectra are dominated by continuum emission produced by the strong electron-ions recombination [1]. For these reasons, the double-pulse approach was proposed [2], where a first laser pulse is used to produce a cavitation bubble at the water-target interface, originating from the expansion of the first plasma plume induced at the target surface, and a second laser pulse produces a second plasma, which expands inside the hot water vapor/gas contained in the bubble. In this way, the cooling process

1559-128X/12/070B30-12$15.00/0

of the second plasma, not affected by the heat conduction of water, is much longer (several microseconds) than the one obtained in water, and the weaker plasma recombination results in a strong reduction of continuum emission and in the appearance of emission lines due to atomic transitions.

Despite the attractiveness of the subject and the widespread possibility of applications, very few groups focused their attention to the investigation of the occurring physical processes, which is necessary for the optimization of the apparatus and for achieving a good control of the measurement process. The peculiarity of the configuration, in fact, makes necessary a better knowledge of many processes, such as the laser ablation in water; the interaction of the laser pulse with water molecules, with water impurities, and with particles produced by plume condensation or laser ablation; the dynamics of the cavitation bubble; the decay of the plasma plume and its interaction with hot vapor, and so on. One of the urging tasks is certainly the improvement of LIBS signal reproducibility [2–5], which is affected by the crater formation, by the gas bubbles formed in the water, and by the interaction of the laser pulse with impurities and particles formed during the ablation process or the plume condensation. The poor reproducibility of double-pulse (DP)-LIBS underwater was previously afforded by Lazic *et al.* [3] by performing a data processing of the spectra, through the selection of those produced by plasmas with similar temperature values; such a method, applied to sediment analysis, allowed one to obtain well correlated calibration curves for several chemical elements (Fe, Ti, Mg, Si) but is, however, severely affected by the difficult estimation of plasma temperature.

One of the reasons for the poor reproducibility of LIBS signal is certainly the shot to shot variation of bubble dimensions, which makes different the environment where the second ablation occurs. It was shown that the dimensions of the cavitation bubble, at the time of the arrival of the second laser pulse, strongly affect LIBS signal both for the different pressure of the vapor inside, which has consequences on the laser ablation process and plasma cooling, and for the different confinement of the second plasma operated by the bubble. In particular, Casavola *et al.* [6] (using two Nd:YAG laser pulses at $\lambda = 532$ nm) showed that higher LIBS signals are obtained for larger bubbles (and correspondingly lower vapor pressures), which is consistent with similar effects obtained in air by using ns laser pulses [7,8]. Then, for a suitable control of the process, it appears essential to determine the experimental conditions able to produce a reproducible cavitation bubble with suitable size and pressure values and with size fluctuations not significantly affecting LIBS signal, together with a good time-stability of the bubble (i.e., in subsequent laser shots) allowing the average of several emission spectra.

The formation and the dynamic evolution of a cavitation bubble inside a liquid environment have been widely studied in the past for their effects and applications in different branches of science and engineering, such as for describing large-scale processes as underwater explosions [9] or describing microscopic phenomena as sonoluminescence [10]. More recently, the generation of a cavitation bubble by a laser pulse focused into the liquid aroused a particular interest in medicine for laser surgery applications [11]. Most of these works, however, deal with cavitation phenomena generated in the bulk of the liquid, eventually near a rigid surface, while a limited number of them focus their attention on the dynamics of a bubble produced by a laser pulse on a metal target immersed in a liquid, as occurring in DP-LIBS. The phenomenon of laser-induced cavitation over a target surface, in fact, significantly differs from the ideal case of a spherical bubble produced in bulk water—on one hand, because the ablation process is determinant for the successive evolution of the bubble, and, on the other, because the interaction of the bubble with the target surface can strongly affect its dynamics via heat or mechanical energy transfer. It is thus evident that the formation and the dynamics of a cavitation bubble over a target surface need dedicated experimental and theoretical investigations, at the moment missing.

From a modeling point of view, cavitation dynamics in bulk water is basically described by the Rayleigh–Plesset equation—which is essentially derived from Navier–Stokes fluidodynamic equations—coupled to a suitable expression accounting for the pressure inside the bubble [10]; however, an accurate description of the phenomenon is complicated by several effects, such as the vaporization-condensation balance at the liquid/vapor interface [12], the heat transfer to the liquid [13,14], the energy loss due to a shock wave emission after the first rebound [12], and, finally, the concomitance of gas and vapor inside the bubble [15], whose amount should be properly estimated. The modeling of the process becomes even more complex when the plasma is induced over a solid surface, where other effects should be considered, such as thermal and mechanical interaction between the bubble and the target surface [16,17], the concomitance of liquid and metal vapor [18], and the nucleation and growth of metal nanoparticles (NPs) that diffuse through the vapor/liquid interface toward the liquid bulk [19]. The complexity of the phenomenon makes it very hard to obtain useful information on the optimal experimental conditions to be used by a theoretical approach, so that a phenomenological approach, followed by a discussion about the relevance of the physical processes occurring, is used in the present work.

Many experimental parameters, including laser pulse duration, energy, and wavelength, as well as target composition, are varied, and their effect on bubble dimensions, reproducibility, and dynamics is investigated. The results, discussed in term of laser ablation process and bubble interaction with the target surface, thus constitute precious preliminary

information for the choice of experimental apparatus to be used in DP-LIBS. After the optimization of the first laser pulse and of the cavitation bubble, a study focused on the LIBS signal optimization is evidently a necessary but successive task, requiring the investigation of the effects related to the second laser pulse (e.g., to the laser ablation, the self-absorption of the lines, the plasma thermodynamic parameters, the interaction with NPs, etc.), and requires a separate and detailed work.

2. Experimental Setup

A shadowgraphy apparatus, as sketched in Fig. 1, was utilized to observe the formation and the dynamical evolution of the cavitation bubble induced on a target surface immersed in water. Two different laser sources, a mode-locked Nd:YAG laser ($\tau = 25$ ps, EKSPLA PL2143A) and a Q-switched Nd:YAG laser ($\tau = 20$ ns, Quanta System CLS 400), both operating at 10 Hz repetition rate, were utilized for the experiment. With both the sources, the measurements were performed both with the fundamental ($\lambda = 1064$ nm) and with the second-harmonic ($\lambda = 532$ nm) emission.

The laser beams were focused slightly below the target surface by means of a 20 cm focal length doublet lens, obtaining a laser spot of approximately 500 μm diameter. With both sources and wavelengths, several fluence values, approximately 2.5, 5, and 7.5 J cm^{-2}, were delivered to the target surface; in order to use the same fluence at different wavelengths, the pulse energies were adjusted to compensate the different absorption of the water layer at 532 and 1064 nm. The fluctuations of laser energy, measured by a thermopile (Gentec ED-200), are of ~5% for both sources. Aluminum and gold plates (purity larger than 99%), used as targets, were placed at the bottom of a 1 cm × 1 cm quartz cuvette, and submerged with twice distilled water up to a liquid depth of 2 cm above the target surface.

Aluminum and gold were chosen because of their markedly different properties characterizing the ablation process, such as the melting points, the ablation thresholds, and the electron-phonon coupling times. The cuvette was installed over a micrometric translational stage to allow the motion of the target shot by shot. The background illumination used for shadowgraphic imaging was provided by a HeNe laser ($\lambda = 632.8$ nm), whose beam profile was properly enlarged by a beam expander, passing through the cuvette in a direction parallel to the target surface. Images were then acquired by a high-speed intensified CCD camera (4 Quick E, Stanford Computer Optics), triggered by the Q-switch output in case of ns laser, and by a digital homemade pulse/delay generator in case of ps laser. At each acquisition delay time, a series of five images, corresponding to five consecutive laser shots, was taken; the acquisition gate was kept constant at 20 ns in all the series. The acquired images were analyzed using the ImageJ software, which allowed the calculation of the bubble radius at each delay time used. Measurements aimed to study the effect of laser-particle interaction were performed at different times during the laser ablation stage (i.e., without changing the water in the cuvette). Differently, for the reconstruction of bubble dynamical evolution, the water in the cuvette was changed every five measurement series in order to avoid effects due to laser absorption/scattering by particles formed in the liquid. For all the experimental conditions, a temporal range of bubble lifetime of 1 ms after laser ablation was spanned. The Size and shape of the craters obtained in different experimental conditions were examined using a ViCo (Biomedica Mangoni and Nikon Instruments, Italy) video-confocal microscope.

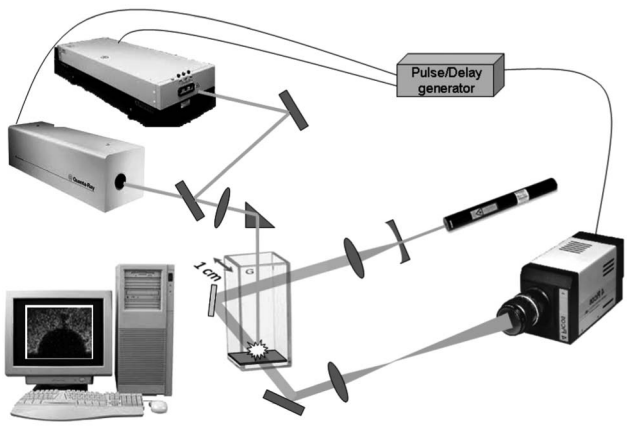

Fig. 1. Experimental setup.

3. Results and Discussion

Shadowgraphic imaging allowed us to observe the laser ablation process and the expansion of the shock waves into the water, and to reconstruct the dynamical evolution of the bubble, from its appearance, around 1 μs, up to 1 ms, passing through several expansion and collapse stages. An illustrative subset of shadowgrams, going from the laser ablation process ($t = 0$) up to 410 μs, including two bubble collapses (at 320 μs and 410 μs), is reported in Fig. 2; the case corresponds to the irradiation of an Al target by a 15 mJ, 20 ns laser pulse at 532 nm. The formation of shock waves and secondary bubbles in the environment is also visible. In the following, three different stages are described and discussed: the laser ablation process, the shock waves evolution, and the cavitation bubble dynamics. The finality of the work (i.e., the optimization of the DP-LIBS apparatus) drove our attention, in particular, at the first and the third stages, which provide information about reproducibility, stability with the number of shots, and evolution of the bubble; the second stage is quickly described for sake of completeness.

A. Stage 1: Laser Ablation

1. *Interaction laser-particles*

The images taken at 0 ns (acquisition delay from the laser firing = −10 ns, gate = 20 ns) show the interaction of the laser pulse with the target and with the particles along its path (Fig. 3). While in

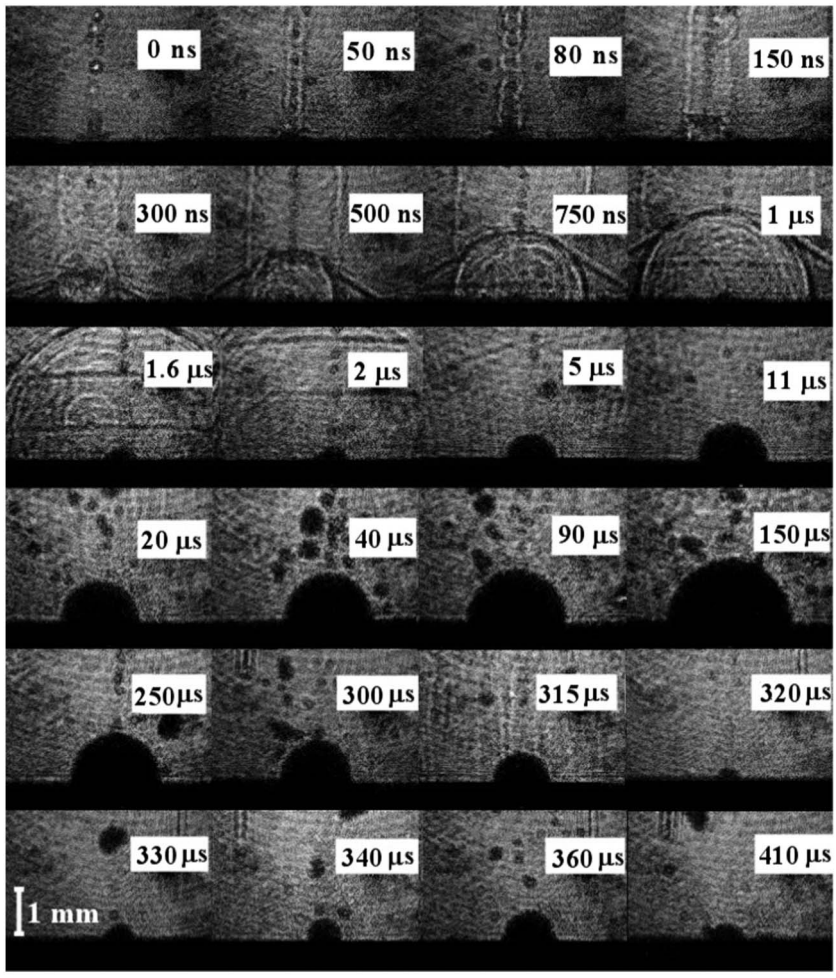

Fig. 2. Shadowgraphic images of laser irradiation of an Al target by a 15 mJ, 532 nm, 20 ns laser pulse.

the case of ns pulses (both for $\lambda = 532$ nm and $\lambda = 1064$ nm), well separated microplasmas are visible along the beam path, similar to that obtained by Kovalchuk *et al.* [20], ps pulses produce a wake inside the medium, as visible in Fig. 3(c). In both cases (Fig. 3(b) and 3(d); see also Fig. 8), shock waves depart from the interaction sites and convolve forming a cylindrical wave. Such features are more marked with increasing the number of laser shots, suggesting that the observed microplasmas and the wake are caused by the interaction with particles, whose concentration in water increases with the number of shots, too. In order to verify such a hypothesis, measurements were repeated in bulk water (i.e., in absence of a solid target), resulting in a strong reduction of both microplasmas and in the disappearance of the wake. Such an outcome indicates that other possible mechanisms, such as laser-interaction with residual impurities present in water (leading to breakdown and plasma formation) and/or change of refractive index of water due to water heating (leading to the formation of a warm channel and a visible wake), play a minor role in producing the observed features.

The formation of particles is a well-known side effect of the laser ablation process in water, where the dimension range of produced particles depends on their originating process. The cooling of the plasma plume results in the nucleation and successive growth of NPs, of dimensions in the range 1–50 nm, which rapidly diffuse in the environment. In conditions similar to our experiment, their formation was demonstrated both for gold [21] and aluminum [22] targets, and, more in general, is exploited for the synthesis of NPs with a widespread range of compositions. Another possible source of particles is phase explosion or hydrodynamic splashing of molten material in the target driven by the pressure exerted by the plasma plume. These mechanisms, commonly observed when laser ablation is performed in air at similar laser fluences [23,24], are due to the ejection of molten drops, and result in the formation of large particles in the *micrometer range*. Hydrodynamic splashing is usually associated with high rims around deep crater holes and is favored in aluminum rather than in gold, because of its lower melting point and ablation threshold. The formation of Al particles in the micrometer range during laser ablation in water was reported by Yan *et al.* [25], where a pulsed KrF excimer laser was used ($\lambda = 248$ nm, $\tau = 30$ ns). In our case, the presence of large particles in Al is suggested by the observation of floating material

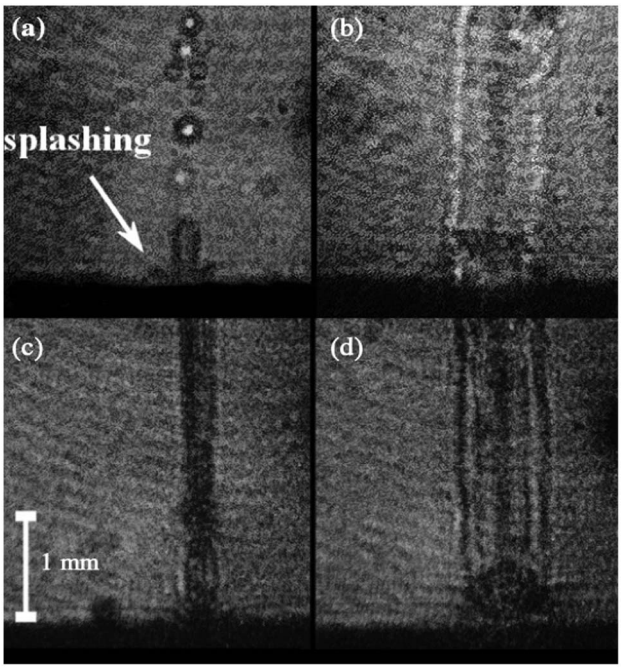

Fig. 3. Laser-pulse interaction with target and particles and subsequent evolution. On the top, $\tau = 20$ ns, $\lambda = 532$ nm at a delay of (a) 0 ns and (b) 150 ns; on the bottom, $\tau = 25$ ps, $\lambda = 1064$ nm at a delay of (c) 0 ns and (d) 150 ns. In order to highlight laser-particles interaction and following shock waves, images are taken after 20–25 shots.

near the target surface, after a few laser shots, since these particles rapidly settle in the proximity of the craters, because of water friction and gravity. The presence of melt splashing in aluminum is also suggested by the depths of the craters and by the size of the rims around them: observation of the craters in Al after 300 laser shots ($\tau = 20$ ns, $\lambda = 1064$ nm) provided a depth of ~300 μm and a rim height of ~100 μm, while in the case of gold, the corresponding values were ~60 μm and ~2 μm. Splashing is also suggested by the lobes near the craters visible in Fig. 3(a) and, to a minor extent, in Fig. 3(c). To conclude, we expect that small NPs are produced both with Al and Au targets, while microparticles are more probably obtained with Al than with Au, because of their different thermal properties.

Both *nano-* and *micro*-particles interact with the incoming laser beam, as predicted by the Mie theory [26], where the relative weight of absorption and scattering depends on the radius of the particles more than on the laser wavelength and on their composition. In the case of NPs, whose dimensions (~1–50 nm) are much smaller than the wavelength, the scattering is negligible, and the main contribution of laser extinction is given by the dipole absorption. Extinction rapidly grows toward the UV region because of the absorption due to the interband transition of the metal. The scattering term becomes considerable for particles in the micrometer range, whose size is comparable with the laser wavelength.

Thus, to explain microplasmas and wakes visible in Fig. 3, we have to focus our attention to the interaction of a laser pulse with NPs diffused in the solution. Many works have been dedicated to this issue both by a theoretical and an experimental approach. The absorption of laser pulses and the following photo-fragmentation of NPs in water has been experimentally verified by measuring the absorbance of the colloid or by transmission electron microscopy (TEM) imaging of NPs before and after laser irradiation [27]. A model of laser-particle interaction was recently proposed in [27], accounting for the laser absorption, for the thermal exchange between the

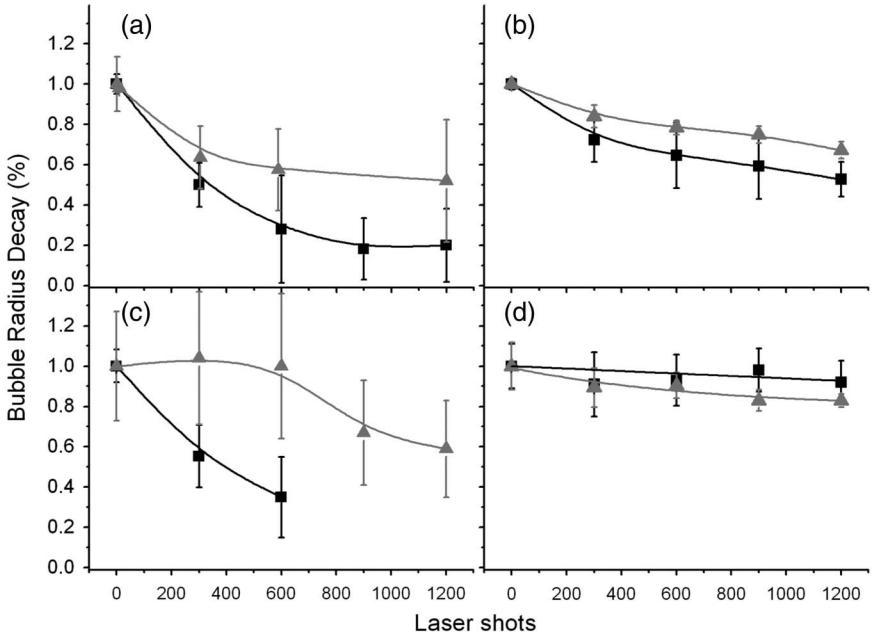

Fig. 4. Percentage decay of the bubble radius (Al target) with the number of laser shots. Squares: $\lambda = 1064$ nm; triangles: $\lambda = 532$ nm. (a) Target fixed, $\tau = 20$ ns; (b) target moving, $\tau = 20$ ns; (c) target fixed, $\tau = 25$ ps; (d) target moving, $\tau = 25$ ps.

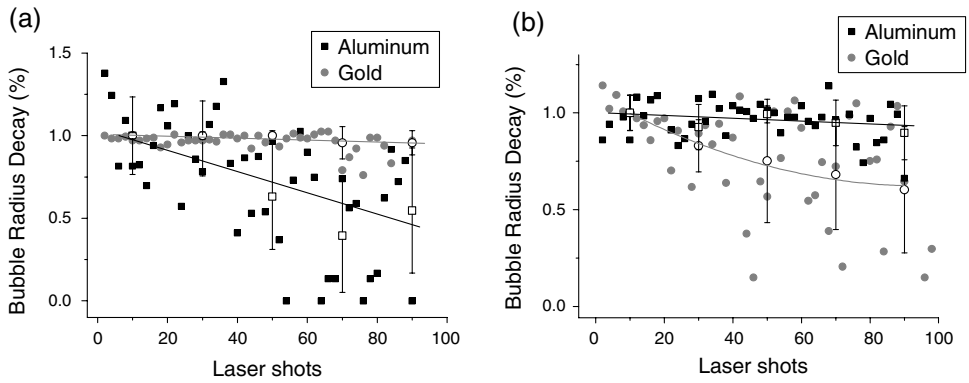

Fig. 5. Percentage decay of the bubble radius induced on Al and Au targets by a nanosecond pulse with elapsing the ablation time. (a) $\lambda = 1064$ nm, target fixed; (b) $\lambda = 532$ nm, target moving.

electrons and the lattice as well as between the NP and the surrounding medium, and for the ejection of electrons via thermoionic emission or multiphoton ionization. Generally speaking, it is possible to say that the interaction strongly depends on the irradiance, the wavelength, and the material properties (e.g., melting point, workfunction, and electron-phonon coupling), which determine if the absorption of photons causes the vaporization of the particle, the ejection of electrons followed by a Coulomb explosion, or both. In the case of gold, it was shown that at low irradiances, as those obtained here by ns pulses ($\sim 5 \cdot 10^8$ W cm^{-2}), thermal effects prevail and particles vaporize and emit electrons by thermoionic effect [28], while, at higher irradiances, as those obtained here by ps pulses ($\sim 5 \cdot 10^{11}$ W cm^{-2}), electrons are emitted via multiphoton ionization [27]. Successively, part of the NP can undergo Coulomb explosion. The bright balls visible in Fig. 3(a) suggest the presence of hot microplasmas, where the breakdown is produced by inverse Bremsstrahlung (IB) processes after which a certain amount of ejected electrons and vaporized atoms are present around the NP. This process is probably absent or less significant in the ps case, because of the short duration of the pulse. In this case, the interaction of the laser pulse with NPs, leading to photo-fragmentation, is, however, testified by the development of shock waves from the interaction sites (Fig. 8).

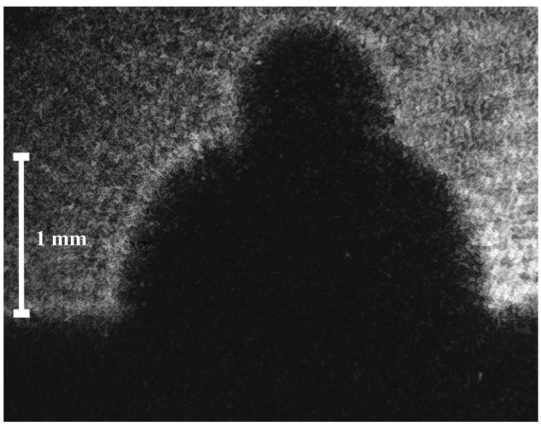

Fig. 6. Bubbles obtained by a picosecond pulse ($\lambda = 532$ nm) followed by a nanosecond pulse ($\lambda = 532$ nm) with a delay of 80 μs. The image is acquired 20 μs after the second pulse.

2. *Reproducibility and time-stability*

The effects of laser-particles interaction as well as of crater formation on the reproducibility and time-stability of the cavitation bubble dimensions were investigated here. In Fig. 4, the decay in the percentage of the bubble radius at maximum expansion with increasing the shot number, obtained for different wavelengths and pulse durations, is reported for an Al target. Frames (a) and (c) refer to the cases where irradiation was made on the same spot, thus affected by crater formation and by the interaction with gas bubbles and particles produced in previous laser shots, while frames (b) and (d) refer to the cases where the target was moved during irradiation. In this second case, results should be affected primarily by the interaction with NPs, which are thought to rapidly diffuse through the liquid [27], since the interaction of the laser pulse with gas bubbles, if not eliminated at all, should at least be strongly reduced. In Table 1, the reproducibility of the bubble radius (in terms of relative standard deviation (RSD) and its time-stability, indicated hereafter as the number of shots necessary to reduce the maximum radius to 90%, are reported. The reduction of bubble dimension leads to an increase of the bubble internal pressure and then, for what concerns DP-LIBS, to a different ablation process induced by the second pulse. It could be useful to have an idea of the variation of the internal pressure at maximum expansion,

Table 1. Reproducibility and Time-Stability of Cavitation Bubble Induced on an Al Target in Different Experimental Conditions

	RSD (%)		Decay to 90% (shots)	
	$\tau = 20$ ns	$\tau = 25$ ps	$\tau = 20$ ns	$\tau = 25$ ps
Target fixed				
$\lambda = 532$ nm	18	27	33 ± 3	150 ± 100
$\lambda = 1064$ nm	30	12	17 ± 2	70 ± 30
Target moving				
$\lambda = 532$ nm	9	7	130 ± 40	180 ± 30
$\lambda = 1064$ nm	10	9	80 ± 20	850 ± 200

when the radius reduces to 90% and 75%. By approximating the bubble as an adiabatic system where gas-vapor follows a polytropic relation $P \propto (R_{max})^{-3\gamma}$, since the adiabatic index γ is in the range 1.33–1.67 (depending on the exact composition of the vapor/gas system), the pressure increases by a factor 1.5–1.7 and 3.4–4.2 when the radius decays to 90% and 75%, respectively. Such estimation, based on the collapse of a single bubble, is evidently an approximate value, since it does not account for possible different laser-couplings and bubble properties induced by pulses of different energies. An accurate investigation of the relation between DP-LIBS signal and bubble pressure is, at the moment, missing in the literature; however, the data reported by Casavola *et al.* [6]—including modeling of bubble pressure evolution and experimental LIBS signal—suggest that a pressure increase by a factor 1.5–1.7 (from 0.6 to 1 atm) corresponds to a decrease of Ti II 353.54 nm and of Ti I 468.19 nm line intensity by an order of magnitude and by a factor 2, respectively. Such results suggest also that the reproducibility of bubble dimensions for DP-LIBS measurements should be evidently better than 10% (i.e., the maximum number of shots used for spectra averaging should be less than that for which the bubble radius at maximum expansion decays to 90%).

Data in Table 1 and Fig. 4 indicate that *focusing on the same spot* leads to a poor reproducibility and time-stability of bubble dimensions. The effect of crater formation—usually including the geometrical variations of the laser fluence, the crater confinement of the plume, and the interaction of ablated species with the crater walls—seems not to play a leading role; in fact, despite the fact that the time-stability seems particularly critical for IR pulses, the corresponding crater depth h is lower or similar to that obtained with visible light (after 300 shots $h_{1064}^{ns} \approx 330$ μm versus $h_{532}^{ns} \approx 560$ μm, $h_{1064}^{ps} \approx 250$ μm versus $h_{532}^{ps} \approx 230$ μm). The poor reproducibility and time-stability could be then attributed in part to the formation of gas bubbles moving toward the water surface. The formation of bubbles appears much more severe when ns laser pulses are used (see Fig. 2); this suggests that the small cavitation bubbles originated by the expansion of microplasmas produced by laser-NPs interaction [Fig. 3(a)] contribute to the total number of gas bubbles in the environment. The scattering of the incoming laser pulse by microparticles near the crater could also contribute to the produce the poor reproducibility obtained with fixed targets.

The comparison of results obtained in Al and Au [see Fig. 5(a)] shows that the reproducibility obtained by focusing on the same spot depends also on the matrix of the target. It can be hypothesized that the higher values of the melting point and ablation threshold of Au, resulting in smaller crater depths and rims, in less splashing, and then in a lower amount of microparticles, are the main causes of the better reproducibility and time-stability of the bubble.

By looking at the results obtained by *moving the target* shot by shot, it is evident that the effect of NPs absorption on the reproducibility and time-stability of the bubble is less dramatic, particularly for ps pulses. The opposite trend observed for the two wavelengths with ns and ps laser pulses (larger decay at 1064 nm for $\tau = 20$ ns, and at 532 nm for $\tau = 25$ ps) can be easily explained by the laser absorption mechanism prevailing in the two cases. While in ps pulses NP absorption prevails, increasing toward the visible and the UV [26], in the case of ns pulses, the laser pulse is strongly absorbed via IB absorption, which is much stronger for IR pulses ($\alpha_{IB} \propto \lambda^3$). Finally, it should be also remarked that the effects of NP interaction depends also on their composition, so that the choice of laser wavelength should be made case by case. As an example, in the case of gold, the radius decay obtained at $\lambda = 532$ nm is dramatic [see Fig. 5(b)], because the strong absorption of Au NPs near the surface plasmon resonance band (peak ~520 nm) strongly reduces the amount of pulse energy reaching the target surface.

3. *Using two laser pulses*

The framework delineated above accounts only for the effects produced by one laser pulse. The reproducibility of the bubble, and then of the environment where the second pulse interacts with the target, is, however, affected also by the *second pulse*. In the present paper, we do not test all the possible configurations that can be utilized, but only two of them, i.e., the cases ps 532 + ns 532 and ns 1064 + ps 1064. In both cases, the interpulse delay was set to 80 μs, corresponding, respectively, to bubble radii of ~1 mm and ~1.6 mm at the arrival of the second pulse. The analysis of the former configuration shows that both reproducibility and time-stability are very similar to that obtained by using only the ps 532 laser pulse (i.e., the first one). However, by looking more carefully at the shadowgraphy images obtained 20 μs after the second laser pulse, it becomes evident that in most of them two bubbles are present, where the second one is formed at the edge of the first one (Fig. 6). Moreover, the dimensions of the main bubble

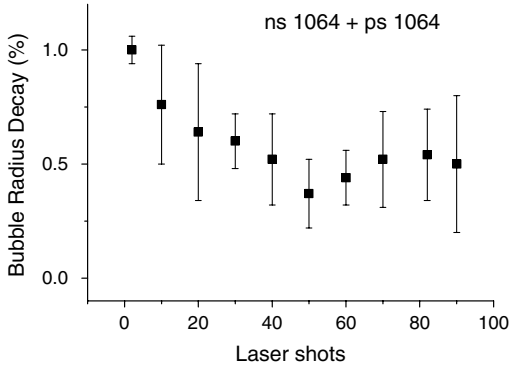

Fig. 7. Time-stability of the bubble radius induced on Al targets by a ns pulse $\lambda = 1064$ nm followed by a ps pulse $\lambda = 1064$ nm. The interpulse delay is 80 μs. The target is moved every shot.

are on average a 10% factor larger when the second bubble is not produced. This suggests that the second laser pulse produces a breakdown at the edge of the first bubble and does not reach the target surface; in cases where this does not occur, the dynamic evolution of the first bubble changes (the dimensions are larger) due to the presence of the second plasma that leads to an enhancement of gas bubble pressure. Although the reason for the breakdown at bubble boundary was not investigated here, one hypothesis relies on the abundance of NPs inside the bubble, maybe attached to the bubble boundaries by the interface tension (as supposed in [25]), which causes absorption and breakdown of the second pulse. The result, though supplementary experimental verifications are needed, suggests that the utilization of a ns laser pulse as second pulse is strongly affected by the interaction with the NPs produced by the first pulse. The second configuration tested (ns 1064 + ps 1064) shows a very poor time-stability and reproducibility, worse than that produced by a single ns pulse (Fig. 7). In this case, after a few shots, the bubble decays to 90%, and thus only few shots could be utilized for measurements. A possible explanation of this result could be the larger production of NPs in this configuration; the hypothesis would agree with the findings of Hahn *et al.* [29], who showed that NPs production in gas (i.e., by the second laser pulse) is ~100 times more than the one in water.

The above cases, though clearly not exhaustive, were reported here to suggest that additional problems should be afforded when a DP-LIBS apparatus is chosen. In particular, the addition of a second pulse certainly requires supplementary and detailed investigations.

B. Stage 2: Shock Waves

Analogously to what happens in air, the laser ablation process drives the formation of shock waves (SWs) both in the target and in the surrounding medium. The latter ones, well visible in Fig. 8, can be subdivided into the following types:

1) The SWs produced by the interaction of the laser pulse with the floating particles. Initially spherical, the SWs rapidly convolve to form a cylindrical SW that expands from the laser beam path.

2) The (emi-) spherical SW produced by the interaction of the laser pulse with the target.

3) The planar SW departing from the surface, produced by the successive rebounds of the SW inside the target. To confirm their origin, in case of aluminum we calculated the sound speed of SWs inside the target by estimating the time elapsed between the appearance on the surface of two successive SWs and by considering the thickness of the Al plate. The resulting value was ~6470 ± 100 m/ sec, which agrees with the literature value of 6420 m/ sec.

4) The oblique SW departing from the laser-surface interaction point. They are target-dependent since they are observed for Al but not for Au targets for both laser sources [Fig. 8(a) and (b)]. One hypothesis for their formation could be the occurrence of splashing of molten material around the crater during the laser ablation, which is much more conspicuous in aluminum than in gold and could compress the surrounding water as a piston.

All the SWs reach the sound speed in water (~1400 m/ sec) in less than 100 ns. A detailed description and analysis of the SWs produced in water are out of the scope of this work; for more details, we direct the reader to other works [30].

C. Stage 3: Bubble Dynamics

The dynamical evolution of the bubbles obtained in the different experimental configurations is reconstructed by the analysis of the shadowgrams. As an example, in Fig. 9, the evolution of the bubble radius induced on an Al target by a 15 mJ, 532 nm, 20 ns laser pulse, which corresponds to the shadowgrams shown in Fig. 2, is reported. The expansion and collapse stages of the main bubble, followed by three rebounds and a successive stage of quasi-equilibrium (radius ~ 300 microns), are visible.

The maximum bubble radius, calculated for all the experimental conditions, is reported in Tables 2 and 3 for IR and visible irradiation, respectively. In the tables is also reported the energy stored in the bubble, estimated by the approximate formula $E_{\mathrm{cav}} = \frac{2}{3}\pi R^3(p_0 - p_b)$, widely used in the literature [10], where p_0 is the atmospheric pressure, p_b is an average bubble pressure, and R is the maximum bubble radius. In the formula, the term $(p_0 - p_b)$ was obtained by the relation $T = 0.915\sqrt{\frac{\rho}{p_0 - p_b}}$, where T is the time corresponding to the first collapse of the bubble and ρ is the density of the liquid.

1. *ns versus ps pulses*

Inspection of Tables 2 and 3 makes evident that the dimensions of the bubble do not only depend on laser energy and wavelength, but also on pulse duration.

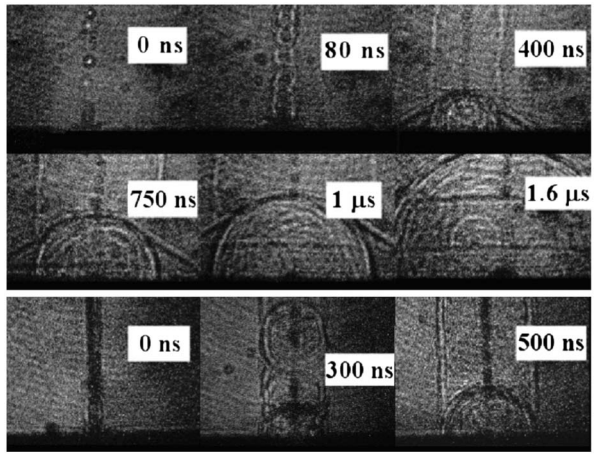

Fig. 8. Shock waves developed during the laser ablation process over (a) Al ($\tau = 20$ ns, $\lambda = 532$ nm) and (b) Au ($\tau = 25$ ps, $\lambda = 1064$ nm) targets. In order to highlight laser-particles interaction and following shock waves, images are taken after 20–25 shots.

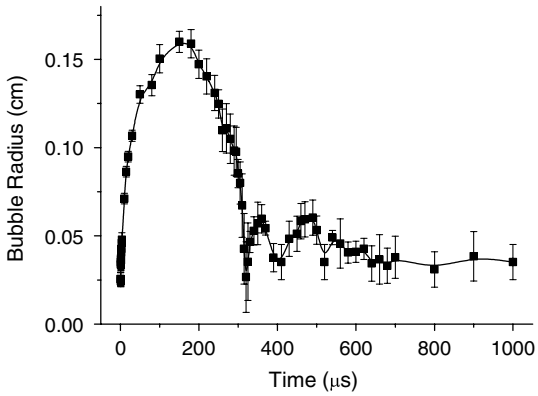

Fig. 9. Time evolution of the cavitation bubble induced on an Al target by a 15 mJ, 532 nm, 20 ns pulse.

The radius and, correspondingly, the percentage of conversion from pulse energy into cavitation energy is generally lower than the values for cavitation induced in bulk water (of the order of a few tens percent), as calculated by Vogel *et al.* [31,32], by 1–2 orders of magnitude. The discrepancy appears much more evident in the case of picosecond laser pulse, where conversion factors as low as a few percent are obtained. Such spread can be explained by the additional channels of energy dissipation in the case of target ablation, including the energy reflected from the surface, the energy spent for melting and vaporizing the solid, the energy dissipated into the target by heat conduction and SWs, and finally the energy consumed into the formation of NPs. The large variation of bubble energy obtained by changing target composition and pulse duration shows that the balancing of these processes can be very different for different experimental configurations, since the laser ablation process can significantly vary case by case. The significant spread between the energies of the bubbles induced by a ps and by a ns laser pulse (see Fig. 10) emphasizes the differences in the ablation process in the two cases.

In the ns case, the plasma absorption (via collisional IB processes) of the laser pulse results in the increase of the temperature of the plasma and in the propagation of the plume in the beam direction via laser-supported mechanisms. The description of the ps ablation process, on the other hand, is much more complex, since the duration of the laser pulse is of the same order of magnitude as the electron-phonon relaxation time. Thus, depending on the laser fluence and on the target composition, melting of the target and evaporation can occur during or after the irradiation [33,34]. Despite that, it was clearly shown by Mao *et al.* [35] for ablation in a gas environment that a plasma forms in front of the target in conjunction with the arrival of the laser pulse, produced by the ionization of air by hot electrons emitted from the target, so that a laser absorption into the plasma exists similarly to the ns case. The occurrence of such a phenomenon in water, however, was not reported in previous publications and is uncertain. Bearing in mind this complex situation, it is plausible that the large bubble radius observed in the case of the ns pulse is due to the larger kinetic energy of atoms in the plume produced by the plasma absorption. The hypothesis agrees with the results of Sakka *et al.* [36], who showed that in the case of a Cu target irradiation by a Q-switched Nd:YAG laser, the bubble radius is larger for longer pulse lengths and,

Table 2. Radius at Maximum Expansion and Energy of the Bubbles Induced on Au and Al Target by 1064 nm Laser Pulses

	R_{max} (cm)	E_{cav} (mJ)	E_{cav}/E_{laser}
	Aluminum		
5 mJ, 20 ns	0.132	0.42	8.4%
10 mJ, 20 ns	0.176	0.95	9.5%
15 mJ, 20 ns	0.214	1.55	10.3%
5 mJ, 25 ps	0.088	0.13	2.5%
10 mJ, 25 ps	0.108	0.19	1.9%
15 mJ, 25 ps	0.111	0.20	1.3%
	Gold		
5 mJ, 20 ns	0.071	0.05	1.1%
10 mJ, 20 ns	0.137	0.33	3.3%
15 mJ, 20 ns	0.165	0.7	4.6%
5 mJ, 25 ps	0.078	0.09	1.2%
10 mJ, 25 ps	0.083	0.08	0.5%
15 mJ, 25 ps	0.091	0.023	0.15%

Table 3. Radius at Maximum Expansion and Energy of the Bubble Induced on Au and Al Target by 532 nm Laser Pulses

	R_{max} (cm)	E_{cav} (mJ)	E_{cav}/E_{laser}
	Aluminum		
5 mJ, 20 ns	0.094	0.13	2.5%
10 mJ, 20 ns	0.14	0.44	4.4%
15 mJ, 20 ns	0.16	0.7	4.5%
5 mJ, 25 ps	0.089	0.13	2.5%
10 mJ, 25 ps	0.1	0.14	1.4%
15 mJ, 25 ps	0.106	0.18	1%
	Gold		
5 mJ, 20 ns	0.047	0.02	0.4%
10 mJ, 20 ns	0.09	0.08	0.8%
15 mJ, 20 ns	0.157	0.29	1.9%
5 mJ, 25 ps	0.058	0.03	0.6%
10 mJ, 25 ps	0.067	0.041	0.4%
15 mJ, 25 ps	0.08	0.05	0.35%

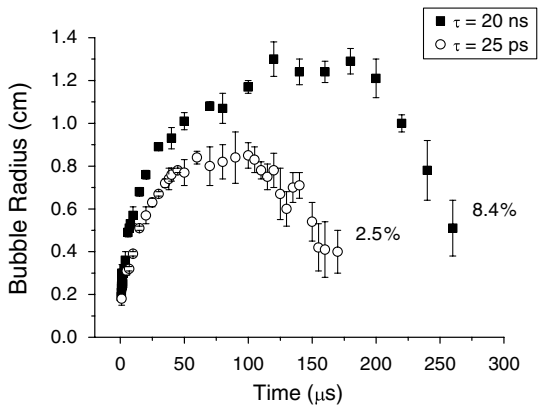

Fig. 10. Time evolution of a cavitation bubble induced on Al target with a 5 mJ/pulse@1064 nm.

simultaneously, the ablation rate is lower. The authors showed that the results depend on the larger plasma shielding occurring for long pulses, producing a little damage on the target but a larger temperature in the plasma. In our results, a confirmation of this picture is constituted by the larger dimensions of bubbles obtained with IR ns with respect to visible ns pulses (Fig. 11) and the growth of energy conversion factors with increasing laser energy (Fig. 12). The former effect is due to the λ^3 scaling of the IB absorption coefficient; the latter depends on the fact that at larger fluences, the plasma shielding begins earlier in the pulse temporal profile, and then a larger portion of it is absorbed [37].

The smaller dimensions of the bubbles induced by ps pulses agree with the lower temperatures observed in ps-fs/plasmas with respect to ns/plasmas [38]. The small differences between the dimensions of the bubble produced by IR and visible pulses cast doubts on the occurrence of plasma collisional absorption in the water environment, which certainly requires a larger energy delivered by hot electrons for its evaporation, dissociation, and ionization. In the case of ps pulses, the conversion factor of laser energy into bubble energy decreases with the fluence. This agrees with the logarithmic scaling of the ablation rate h with the fluence [33,34], expressed by $h = k\ \ln(\Phi/\Phi_{\text{thres}})$, where Φ_{thres} is the ablation threshold and the coefficient k is equal to the optical penetration depth in the low fluence regime and to the electron heat diffusion depth in the high fluence regime. In fact, if laser absorption into the plasma is absent, the increase of temperature with the fluence is not relevant, and then the scaling of bubble energy with the laser energy is given by the amount of atoms in the plume and then by the ablation rate.

2. *Target composition*

Tables 2 and 3 are evidence of a strong dependence of bubble dimensions on the composition of the target, where bubble radii for Al are significantly larger than for Au (e.g., see Fig. 13). This result could be put in relation to the significantly different ablation yield in the two cases, resulting in deeper craters in aluminum, as usually reported in the literature [33,39].

The difference in the ablation process is due to different properties of the two materials, such as, for example, the reflectivity, the electron-phonon coupling time, and the melting point. The reflectivity of gold at 1064 nm is significantly larger (~99%) than that of aluminum (~95%), so that the energy transmitted to the bulk is five times larger in the latter case; however, the trend is opposite at 532 nm, where the reflectivity of gold (~75%) is lower than that of aluminum (~92%). Also the difference between electron-phonon (e-p) coupling times ($\tau_{\text{Al}} = 4$ ps, $\tau_{\text{Au}} = 119$ ps) and melting points ($T_{\text{Al}} = 933$ K, $T_{\text{Au}} = 1337$ K) is significant, resulting in a larger ablation threshold of gold. The different e-p coupling times indicate that laser ablation by a ps pulse can be considered "cold" in the case of gold, where the melting and the evaporation of the target occurs after the end of the laser pulse; conversely, in aluminum, the pulse interacts with the molten surface. At first glance, the difference in reflectivity could explain the different bubble radius obtained for Au and Al at 1064 nm irradiation; however, in this picture, one should also expect the opposite trend

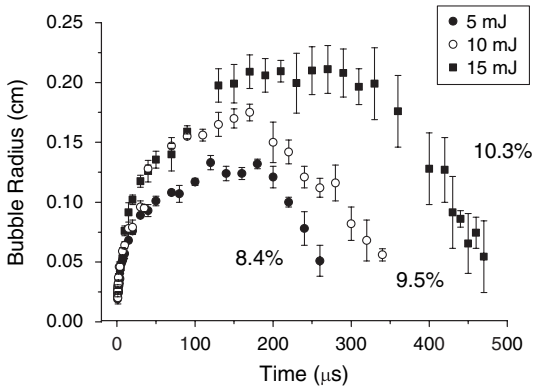

Fig. 12. Time evolution of bubbles induced on Al target with a 1064 nm, 20 ns laser pulse. The percentage of pulse energy converted into bubble energy is reported beside each curve.

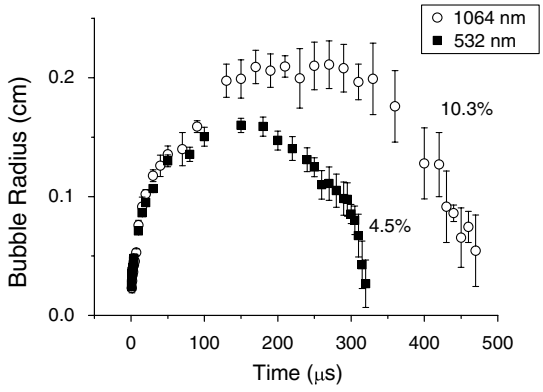

Fig. 11. Bubble dynamics in the cases Al target 15 mJ pulse $\tau = 20$ ns. Beside the curves, the percentage of pulse energy converted into bubble energy is reported.

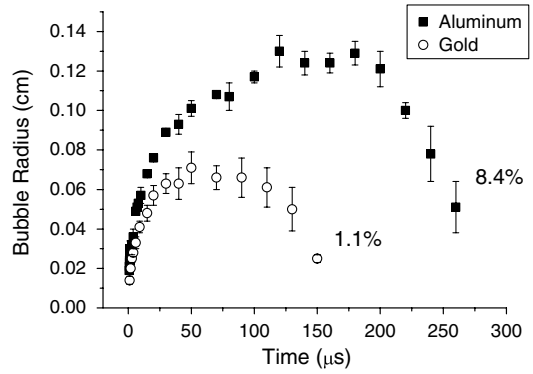

Fig. 13. Time evolution of bubbles induced on Al and Au targets with a 1064 nm, 5 mJ, 20 ns laser pulse.

at 532 nm, at least for ps ablation, where plasma absorption is probably absent. Actually, the different reflectivity can play a role only at the very early stage of the ablation process, since the rapid growth of electron temperature into the target surface results in a rapid decrease of the reflectivity [39] up to values typical of dielectrics near the phase explosion threshold [40]. Thus, the smaller bubbles in case of gold are rather related to the larger ablation threshold and rate, resulting in less ablated atoms and in a smaller initial pressure of the bubble. In the case of ns laser ablation, the lower ionization energy of Al can also play a role, resulting in a faster supply of electrons to ignite the plasma absorption via the IB process.

4. Concluding Remarks: What Can We Learn for DP-LIBS?

The DP-LIBS in water, proposed and tested for analytical measurements of samples located underwater, usually suffers from a poor reproducibility and a rapid fall of the spectroscopic signal with the number of shots. Driven by the needs of reducing these drawbacks, the present work was focused on investigating the effects limiting the reproducibility of the cavitation bubble induced by the first laser pulse, which affects the reproducibility of the final LIBS measurement, and on determining the experimental conditions able to improve it. Aside from the effects due to the drilling of a crater on the target surface, the reproducibility of the laser ablation process in the liquid environment is limited by the formation of particles, which produce absorption and scattering of the laser beam, and of gas bubbles, which can induce its focusing/defocusing and path deviations. In turn, both the crater formation and the formation of particles are dependent on the matrix of the target analyzed, which makes even more complex the choice of which experimental condition to utilize. Moving the target or the laser beam shot by shot removes the effects produced by the crater and strongly reduces those due to gas bubbles, moving toward the liquid surface, and to micrometer particles, which mainly remain in the area around the crater. This solution leads to a reduction of bubble radius RSD by a factor 2–3 and to a much higher time-stability, especially when IR pulses are utilized. The effect of NPs, which absorb part of the laser beam and successively vaporize or undergo Coulomb explosion, cannot be eliminated by changing the area of the laser ablation, since they rapidly diffuse in the surrounding environment. Their effect is, however, smaller (RSD less than 10% and time-stability better than 100 shots) when ps pulses are used. When operating in a large liquid environment (as in-situ undermarine measurements), these factors of merit can probably be improved by mechanically flushing away the NPs during the measurement.

A better performance of ps laser pulses is found (both for RSD and time-stability), which is due to the different interaction with the target and with the NPs, where the absorption of photons is followed, but separate in time, by the ablation. Differently, the ablation of ns pulses is a plasma-mediated process where the trailing part of the pulse is absorbed by the plasma, which can also etch directly the target surface. The interaction of ns pulses with the sample surface leads to larger bubbles (with lower internal pressures), especially when utilizing IR pulses, due to the occurrence of laser-supported mechanisms. This effect, which would be favorable for LIBS measurements, is, however, associated to a worst reproducibility, caused by the stronger absorption of the laser pulse by the floating NPs, since the laser absorption by the plasma generated around the particle adds to the absorption of conduction electrons inside the NP itself. The laser-NPs interaction results also in the formation of gas bubbles, especially for IR pulses. The relevance of NPs interaction with ns pulses also casts doubts on their utilization as second pulses, as suggested by preliminary double-pulse tests performed in the case of ps 532 + ns 532 combination.

When using ps pulses and the target is kept in motion, the utilization of 1064 nm emission is suggested, since it is less affected by NPs absorption and provides larger bubble time-stability associated to comparable values of RSD and bubble dimensions.

In conclusion, the results suggest that a careful choice of experimental conditions should be done case by case, depending on the matrix of the sample to analyze. Ps laser pulses emitting at IR wavelength seem to be preferable for inducing stable and reproducible bubbles and also for inducing the second laser ablation into the bubble.

Future work is needed to verify whether the dimensions of the bubbles induced by ps pulses (as first pulse) are large enough for producing an internal pressure suitable for LIBS measurements and at the same time a suitable confinement of the second plasma. Spectroscopic measurements are needed to verify whether LIBS signal induced by ps pulses (as second pulse) is high enough for achieving limits of detection significant for applications. An accurate model of bubble dynamics, including, at least, thermal effects, NPs formation, and gas content, and able to describe the thermodynamics of the vapor/gas inside the cavitation, could also help to determine the relation between the LIBS signal and the thermodynamic conditions of the bubble content.

F. Giammanco, M. Tiberi, A Simonelli, and P. Marsili wish to acknowledge funding from the project NABLA (Decree n.4508, September 1, 2010, by Regione Toscana-Italy, PAR FAS 2007–2013 funds, Action 1.1.a.3).

References

1. A. De Giacomo, M. Dell'Aglio, O. De Pascale, and M. Capitelli, "From single pulse to double pulse ns-laser induced breakdown spectroscopy under water: elemental analysis of aqueous solutions and submerged solid samples," Spectrochim. Acta B **62**, 721–738 (2007).

2. A. E. Pichahchy, D. A. Cremers, and M. J. Ferris, "Elemental analysis of metals under water using laser-induced breakdown spectroscopy," Spectrochim. Acta B **52**, 25–39 (1997).
3. V. Lazic, F. Colao, R. Fantoni, V. Spizzichino, and S. Jovicevic, "Underwater sediment analyses by laser induced breakdown spectroscopy and calibration procedure for fluctuating plasma parameters," Spectrochim. Acta B **62**, 30–39 (2007).
4. V. Lazic, F. Colao, R. Fantoni, and V. Spizzicchino, "Recognition of archeological materials underwater by laser induced breakdown spectroscopy," Spectrochim. Acta B **60**, 1014–1024 (2005).
5. V. Lazic, F. Colao, R. Fantoni, and V. Spizzicchino, "Laser-induced breakdown spectroscopy in water: improvement of the detection threshold by signal processing," Spectrochim. Acta B **60**, 1002–1013 (2005).
6. A. Casavola, A. De Giacomo, M. DellAglio, F. Taccogna, G. Colonna, O. De Pascale, and S. Longo, "Experimental investigation and modeling of double pulse laser induced plasma spectroscopy under water," Spectrochim. Acta B **60**, 975–985 (2005).
7. G. Cristoforetti, S. Legnaioli, V. Palleschi, A. Salvetti, and E. Tognoni, "Influence of ambient gas pressure on laser induced breakdown spectroscopy technique in the parallel double pulse configuration," Spectrochim. Acta B **59**, 1907–1917 (2004).
8. Y. Iida, "Effects of atmosphere on laser vaporization and excitation processes of solid samples," Spectrochim. Acta B **45**, 1353–1367 (1990).
9. R. H. Cole, *Underwater Explosions* (Princeton University, 1948).
10. M. P. Brenner, S. Hilgenfeldt, and D. Lohse, "Single-bubble sonoluminescence," Rev. Mod. Phys. **74**, 425–484 (2002).
11. T. Juhasz, G. A. Kastis, C. Sudrez, Z. Bor, and W. E. Bron, "Time-resolved observations of shock waves and cavitation bubbles generated by femtosecond laser pulses in corneal tissue and water," Lasers Surg. Med. **19**, 23–31 (1996).
12. I. Akhatov, O. Lindau, A. Topolnikov, R. Mettin, N. Vakhitova, and W. Lauterborn, "Collapse and rebound of a laser-induced cavitation bubble," Phys. Fluids **13**, 2805–2819 (2001).
13. B. Han, B. Yang, R. Zhao, H. C. Zhang, Z. H. Shen, J. Lu, and X. W. Ni, "The influence of thermodynamic gas parameters on laser-induced bubble dynamics in water," Eur. J. Mech. B, Fluids **29**, 430–434 (2010).
14. W. K. Soh and A. A. Karimi, "On a calculation of heat transfer in a pulsating bubble," Appl. Math. Model. **20**, 638–645 (1996).
15. C. E. Brennen, *Cavitation and Bubble Dynamics* (Oxford University, 1995).
16. N. Takada, T. Nakano, and K. Sasaki, "Formation of cavitation-induced pits on target surface in liquid-phase laser ablation," Appl. Phys. A **101**, 255–258 (2010).
17. J. C. Isselin, A. P. Alloncle, and M. Autric, "On laser induced single bubble near a solid boundary: contribution to the understanding of erosion phenomena," J. Appl. Phys. **84**, 5766–5771 (1998).
18. R. Xu, R. Zhao, Y. Cui, J. Lu, and X. Ni, "The collapse and rebound of gas-vapour cavity on metal surface," Optik **120**, 115–120 (2009).
19. T. Tsuji, Y. Tsuboi, N. Kitamura, and M. Tsuji, "Microsecond-resolved imaging of laser ablation at solid-liquid interface: investigation of formation process of nano-size metal colloids," Appl. Surf. Sci. **229**, 365–371 (2004).
20. T. Kovalchuk, G. Toker, V. Bulatov, and I. Schechter, "Laser breakdown in alcohols and water induced by $\lambda = 1064$ nm nanosecond pulses," Chem. Phys. Lett. **500**, 242–250 (2010).
21. G. Compagnini, A. A. Scalisi, and O. Puglisi, "Ablation of noble metals in liquids: a method to obtain nanoparticles in a thin polymeric film," Phys. Chem. Chem. Phys. **4**, 2787–2791 (2002).
22. B. Kumar and R. K. Thareja, "Synthesis of nanoparticles in laser ablation of aluminium in liquid," J. Appl. Phys. **108**, 064906 (2010).
23. C. Porneala and D. A. Willis, "Observation of nanosecond laser-induced phase explosion in aluminum," Appl. Phys. Lett. **89**, 211121 (2006).
24. G. Cristoforetti, S. Legnaioli, V. Palleschi, E. Tognoni, and P. A. Benedetti, "Observation of different mass removal regimes during the laser ablation of an aluminium target in air," J. Anal. At. Spectrom. **23**, 1518–1528 (2008).
25. Z. Yan, R. Bao, Y. Huang, and D. B. Chrisey, "Hollow particles formed on laser-induced bubbles by excimer laser ablation of Al in liquid," J. Phys. Chem. C **114**, 11370–11374 (2010).
26. U. Kreibig and M. Vollmer, *Optical Properties of Metal Clusters* (Springer, 1995).
27. F. Giammanco, E. Giorgietti, P. Marsili, and A. Giusti, "Experimental and theoretical analysis of photofragmentation of Au nanoparticles by picosecond laser radiation," J. Phys. Chem. C **114**, 3354–3363 (2010).
28. K. Yamada, K. Miyajima, and F. Mafuné, "Thermionic emission of electrons from gold nanoparticles by nanosecond pulse-laser excitation of interband," J. Phys. Chem. C **111**, 11246–11251 (2007).
29. A. Hahn, S. Barcikowski, and B. N. Chichkov, "Influences on nanoparticle production during pulsed laser ablation," J. Laser Micro/Nanoeng. **3**, 73–77 (2008).
30. L. Martí-López, R. Ocaña, J. A. Porro, M. Morales, and J. L. Ocaña, "Optical observation of shock waves and cavitation bubbles in high intensity laser-induced shock processes," Appl. Opt. **48**, 3671–3680 (2009).
31. A. Vogel, J. Noack, K. Nahen, D. Theisen, S. Busch, U. Parlitz, D. X. Hammer, G. D. Noojin, B. A. Rockwell, and R. Birngruber, "Energy balance of optical breakdown in water at nanosecond to femtosecond time scales," Appl. Phys. B **68**, 271–280 (1999).
32. A. Vogel, S. Busch, and U. Parlitz, "Shock wave emission and cavitation bubble generation by picosecond and nanosecond optical breakdown in water," J. Acoust. Soc. Am. **100**, 148–165 (1996).
33. J. Cheng, W. Perrie, M. Sharp, S. P. Edwardson, N. G. Semaltianos, G. Dearden, and K. G. Watkins, "Single-pulse drilling study on Au, Al, and Ti alloy by using a picosecond laser," Appl. Phys. A **95**, 739–746 (2009).
34. J. Bonse, J. M. Wrobel, J. Kruger, and W. Kautek, "Ultrashort-pulse laser ablation of indium phosphide in air," Appl. Phys. A **72**, 89–94 (2001).
35. S. S. Mao, X. Mao, R. Greif, and R. E. Russo, "Initiation of an early-stage plasma during picosecond laser ablation of solids," Appl. Phys. Lett. **77**, 2464–2466 (2000).
36. T. Sakka, F. Masai, K. Fukami, and Y. H. Ogata, "Spectral profile of atomic emission lines and effects of pulse duration on laser ablation in liquid," Spectrochim. Acta B **64**, 981–985 (2009).
37. A. Bogaerts, Z. Chen, R. Gijbels, and A. Vertes, "Laser ablation for analytical sampling: what can we learn from modeling?," Spectrochim. Acta B **58**, 1867–1893 (2003).
38. P. Stavropoulos, C. Palagas, G. N. Angelopoulos, D. N. Papamantellos, and S. Couris, "Calibration measurements in laser-induced breakdown spectroscopy using nanosecond and picosecond lasers," Spectrochim. Acta B **59**, 1885–1892 (2004).
39. K. Ujihara, "Reflectivity of metals at high temperatures," J. Appl. Phys. **43**, 2376–2383 (1972).
40. A. Miotello and R. Kelly, "Critical assessment of thermal models for laser sputtering at high fluences," Appl. Phys. Lett. **67**, 3535–3537 (1995).